ACS NANO

www.acsnano.org

ARTICLE

Accelerated Bone Regeneration by Two-Photon Photoactivated Carbon Nitride Nanosheets

Jitendra N. Tiwari,[†,‡] Young-Kyo Seo,[§,‡] Taeseung Yoon,[†] Wang Geun Lee,[†] Woo Jong Cho,[†] Muhammad Yousuf,[†] Ahmad M. Harzandi,[†] Du-Seok Kang,[§] Kwang-Youn Kim,[§] Pann-Ghill Suh,[*,§] and Kwang S. Kim[*,†]

[†]Department of Chemistry and [§]School of Life Sciences, Ulsan National Institute of Science and Technology (UNIST), 50 UNIST-gil, Ulsan 44919, Korea

Supporting Information

ABSTRACT: **Human bone marrow-derived mesenchymal stem cells (hBMSCs) present promising opportunities for therapeutic medicine. Carbon derivatives showed only marginal enhancement in stem cell differentiation toward bone formation. Here we report that red-light absorbing carbon nitride (C_3N_4) sheets lead to remarkable proliferation and osteogenic differentiation by runt-related transcription factor 2 (Runx2) activation, a key transcription factor associated with osteoblast differentiation. Accordingly, highly effective hBMSCs-driven mice bone regeneration under red light is achieved (91% recovery after 4 weeks compared to 36% recovery in the standard control group in phosphate-buffered saline without red light). This fast bone regeneration is attributed to the deep penetration strength of red light into cellular membranes *via* tissue and the resulting efficient cell stimulation by enhanced photocurrent upon two-photon excitation of C_3N_4 sheets near cells. Given that the photoinduced charge transfer can increase cytosolic Ca^{2+} accumulation, this increase would promote nucleotide synthesis and cellular proliferation/differentiation. The cell stimulation enhances hBMSC differentiation toward bone formation, demonstrating the therapeutic potential of near-infrared two-photon absorption of C_3N_4 sheets in bone regeneration and fracture healing.**

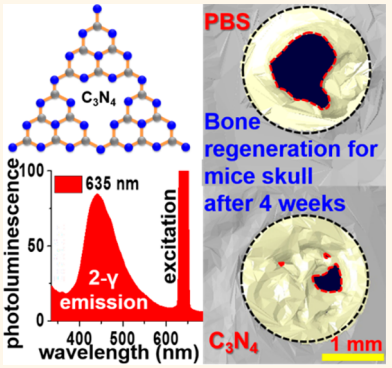

KEYWORDS: *two-photon materials, carbon nitride nanosheets, mesenchymal stem cells, proliferation, osteogenic differentiation, bone regeneration*

A great deal of research has been focused on human bone regeneration.[1−5] Human bone marrow-derived mesenchymal stem cells (hBMSCs) can revolutionize medicine with their innate ability to regenerate bones and heal fractures.[6−11] However, *in vivo* tests show that the tedious and time-consuming cellular transplantations result in low survival colonization and low differentiation.[12,13] Biomaterials have been applied as supportive means for controlled factor release or as a temporary extracellular matrix (ECM) substitute to cells in tissue engineering. However, these materials have not led to satisfactory bone regeneration. Cancellous bone grafts, which are the clinical standard, have underlying problems such as limited availability, donor site morbidity, and inflammatory risks. The two-dimensional (2D) nanomaterials such as clays (nanosilicates), hexagonal boron nitride, carbon nitride, and layered double hydroxides have been used for biomedical applications.[14] More recently, carbon derivatives, such as carbon dots, carbon nanotubes, graphene and its oxide, are shown to enhance stem cells differentiation.[15−23]

Yet, these materials display less promising toward bone formation due to photobleaching and phototoxicity effects.[24] In this regard, it is critically important to discover new bone fracture and/or regeneration approaches and useful materials that are simple, rapid, and nontoxic.

Since ultraviolet light is known to be harmful by causing skin cancer, two-photon absorption has not been considered as a possible medical treatment. However, here we report the demonstration of the superb two-photon steered bone regeneration using red light. It can be attributed to the deep penetration strength of red light into cellular membranes *via* tissue[25−28] and the cell stimulation by two-photon steered photocurrent, which translocates Ca^{2+} and increases cytosolic Ca^{2+}, upon two-photon excitation of C_3N_4 sheets near cells.[29]

Received: October 22, 2016
Accepted: December 29, 2016
Published: December 29, 2016

DOI: 10.1021/acsnano.6b07138
ACS Nano 2017, 11, 742−751

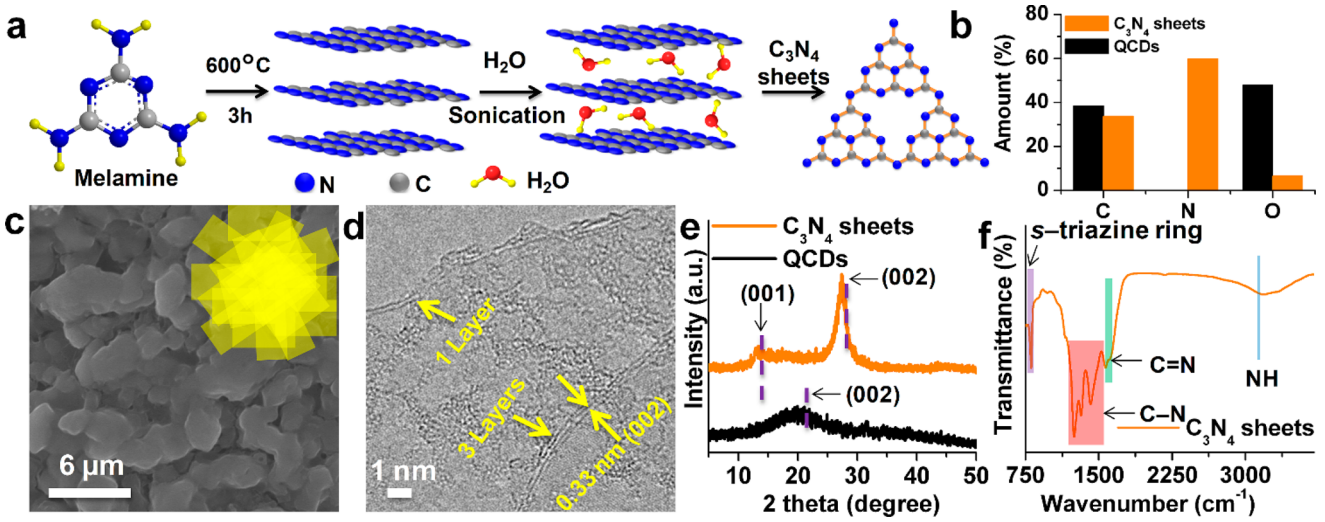

Figure 1. Synthesis and characterization of C_3N_4 sheets. (a) Synthetic procedure. (b) EDX analysis. (c) SEM image (inset shows the layer-by-layer overlapping structure of assembled C_3N_4 sheets). (d) HRTEM image of liquid exfoliated bulk C_3N_4 in water. (e) XRD and (f) FTIR spectra.

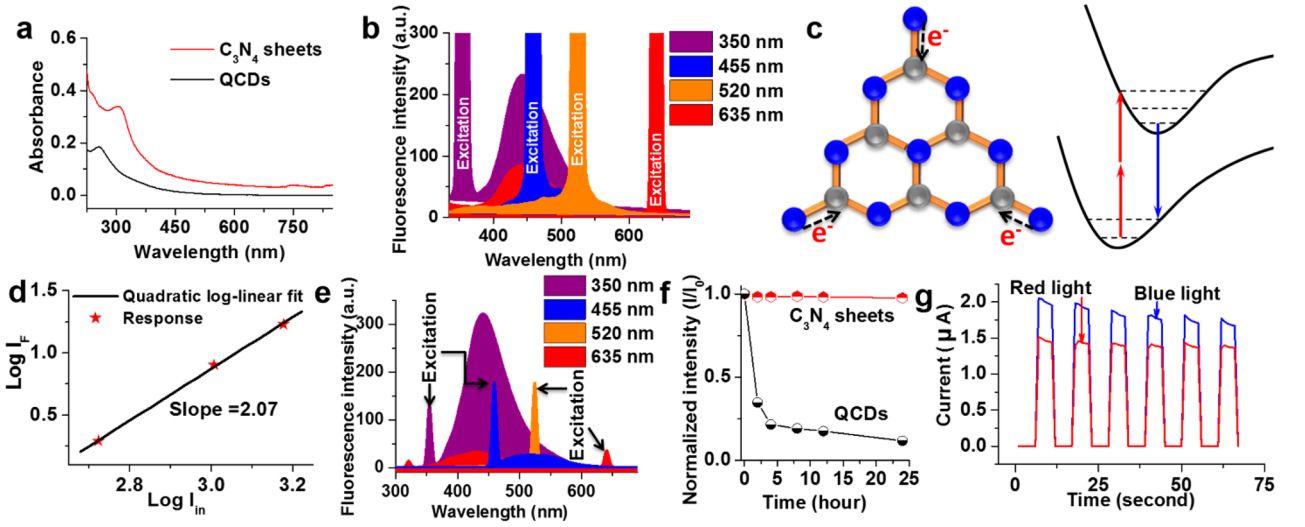

Figure 2. Optical properties, two-photon absorption and photocurrent. (a) UV–vis absorption spectra. (b) Two-photon fluorescence spectra for the C_3N_4 sheets dispersed in water at different excitation wavelengths. (Upon excitation at 350 nm, the fluorescence peak appears at 440 nm. Even for 635 nm, the fluorescence peak appears at 440 nm, indicating the two-photon absorption.) (c) Two-photon fluorescence mechanism for C_3N_4. (d) Fluorescence signal as a function of incident irradiance intensity, the slope (~2.07) of which demonstrates a two-photon active process. (e) Fluorescence spectra for the quantum-sized carbon dots (QCDs) dispersed in water at different excitation wavelengths. (f) Photobleaching test. (g) Photocurrent transients measured under intensity modulated blue and red light.

RESULTS AND DISCUSSION

The synthetic procedure for C_3N_4 sheets is displayed in Figure 1a (see Experimental Section and Supporting Information text for further details). Energy dispersive X-ray (EDX) analysis indicates a chemical composition ratio ~1.78 for N:C (Figure 1b), consistent with the X-ray photoelectron spectroscopy (XPS) survey spectra obtained for the C_3N_4 sheets (Figure S6a in Supporting Information). Scanning electron microscopy (SEM) images indicate that the C_3N_4 particles with an average size of ~6 μm are formed by the random stacking of individual sheets (Figure 1c). High-resolution transmission electron microscopy (HRTEM) shows that the exfoliated C_3N_4 sheets are composed of one to three C_3N_4 layers with a lattice spacing of ~0.33 nm corresponding to the (002) plane (Figure 1d). The strong peak located at 27° in the X-ray diffraction (XRD) patterns could be indexed to the (002) plane (Figure 1e), while the weak peak at 13° can be assigned to the (001) plane. The interlayer distance (002 plane) of C_3N_4 layers using scherrer formula is ~0.329 nm, which is very similar to the HRTEM value 0.33 nm.

The presence of *s*-triazine rings in C_3N_4 sheets is confirmed by a UV–vis absorption peak around ~305 nm ($\pi \rightarrow \pi^*$ electronic transition;[30] Figure 2a) as well as a Fourier-transformed infrared (FTIR) sharp peak at 807 cm^{-1} corresponding to the *s*-triazine ring (Figure 1f). The quantum-sized carbon dots (QCDs) show an absorption band at ~256 nm (Figures 2a and S3–6) due to the π–π^* transition of graphitic sp^2 domains, which supports a high degree of carbonization in the aromatic core through restrained nonradiative recombination. The C_3N_4 sheets show higher absorption in the UV, visible, and NIR regions than QCDs,

DOI: 10.1021/acsnano.6b07138
ACS Nano 2017, 11, 742–751

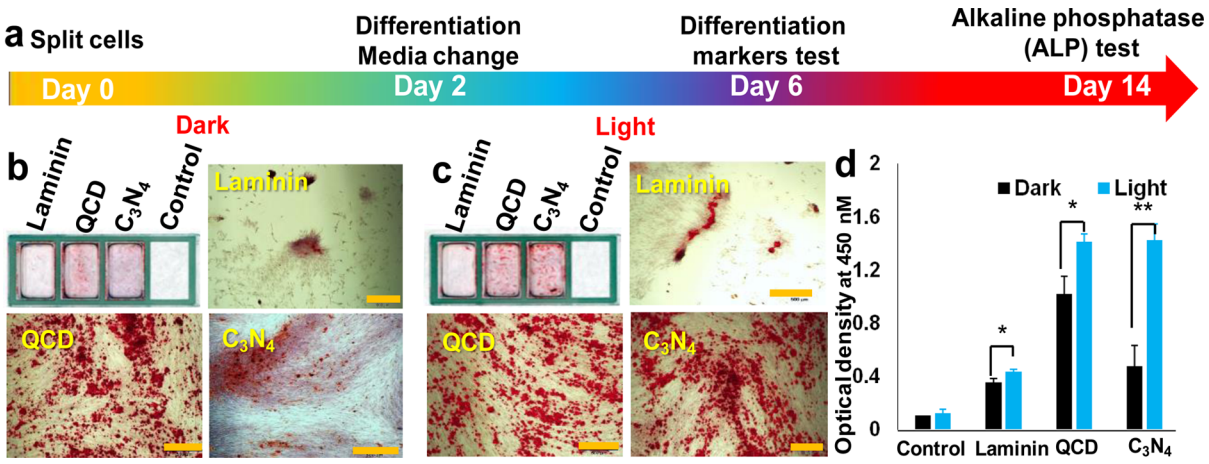

Figure 3. Alizarin red staining of hBMSCs seeded on laminin, QCDs, C_3N_4 sheets, and control. (a) Schematic diagram illustrating experimental design and time course. A higher amount of Alizarin red, which is an indicator of osteogenic differentiation, is found in hBMSCs cultured on (b) dark and (c) light conditions for 14 days in osteogenic differentiation medium. (d) ALP activity was measured at OD at 450 nm after 14 days. Scale bar, 500 μm. All figures are representative of 3 separate experiments (*p < 0.1, **p < 0.001).

indicating that C_3N_4 sheets are more polarized with more electron–hole pairs (Figure 2a).

The fluorescences of C_3N_4 sheets and QCDs are studied. When the C_3N_4 sheets are excited at 350 nm, a broad photoluminescence (PL) emission peak centered at ~443 nm (blue line) appears (Figure 2b) with a PL quantum yield (QY) of 26.8% with respect to an anthracene reference (see Experimental Section and Table S1). Upon excitation at 455 and 520 nm, the PL emission peak could not be determined precisely due to the decreased mean PL intensity. However, upon excitation at ~635 nm, a strong two-photon-driven PL emission centered at ~443 nm appears (Figure 2b) with QY 14.3%. Upon excitation at longer wavelengths, the simultaneous absorption of two photons leads to the same PL emission centered at ~443 nm, a much shorter wavelength than the excitation wavelength[31,32] (Figure S7), confirming a two-photon fluorescence emission in C_3N_4 sheets (Figure 2d). In contrast, QCDs exhibit a much weaker QY (12.9% at 350 nm, 7.4% at 635 nm) (Figure 2e and Table S1). Highly π-conjugated polyaromatic C_3N_4 sheets show fluorescence through π–π* electron transitions (Figure 2c).[24] The large π-conjugation in C_3N_4 sheets and strong donating effect of amino groups provide rapid electron transfer and easy thermal transfer, thereby allowing a two-photon-induced fluorescence in the C_3N_4 sheets.[33] The C_3N_4 sheets emit blue fluorescence upon UV-light radiation, and their fluorescence intensity is stable without significant photobleaching loss even after irradiation with a UV-light for 24 h. In contrast, QCDs exhibit a large photobleaching effect (~80% degradation after 5 h) (Figure 2f). Under continuous irradiation (2 h), the temperature of an aqueous solution of dispersed C_3N_4 sheets (400 μg mL^{-1}) increases only by ~5 °C, akin to the pure water case, suggesting a negligible photothermal effect (Figure S8).

We measured the transient photocurrent of C_3N_4 sheets in the presence of blue/red light (Figure 2g). Since the band gap of C_3N_4 sheets is 2.7 eV (460 nm),[34] one could expect that it can be excited by blue light, but not by red light. However, C_3N_4 sheets show strong nonlinear optical effects. Upon the exposure of red light, C_3N_4 sheets allow two-photon excitation with red light (quantum yield 14.3% for 635 nm), and then the resulting fluorescence releases electrons, generating photocurrent. The red-light-driven photocurrent is almost as strong as the blue-light-driven photocurrent.

To evaluate their biocompatibility, a methyl thiazolyl tetrazolium (MTT)-based cytotoxicity assay was performed with C_3N_4 sheets and QCDs. HeLa cells have high viabilities in a 200 μg mL^{-1} concentrations of aqueous C_3N_4 sheets (more than 96%) and QCDs (~95%) (Figures S9 and S10).

To reduce the possible artifacts associated with MTT assay, Trypan blue staining,[35] and fluorescence-activated cell sorting (FACS) analyses[36] are used to measure the cell viability. Even at higher concentrations, C_3N_4 sheets show little toxicity to HeLa cells (Figures S11 and S12). The large fluorescence intensity, two-photon steered photocurrent, good water dispersibility, negligible photothermal effect, and remarkable biocompatibility of the C_3N_4 sheets permit *in vitro* and *in vivo* bioapplications of these C_3N_4 sheets without cytotoxicity (Figures S1 and S9–S12). Accordingly, we studied the effect of C_3N_4 sheets on hBMSC differentiation and bone regeneration in the presence/absence of irradiation.

Phosphate-buffered saline (PBS), laminin, QCDs, and C_3N_4 sheets are used to grow and differentiate hBMSCs (Figure S13). To provide adhesion to the growth plates, a laminin coating (10 μg mL^{-1} for 4 h) is required for QCDs and C_3N_4 sheets samples. The hBMSC differentiation with respect to time for the test and control samples is studied (Figure 3a). The hBMSCs are seeded on the growth plate, and the osteogenic differentiation is investigated in the presence/absence of irradiation for 14 days. A dark-red color is observed for the C_3N_4-coated plate when irradiated and stained with alizarin red. This color change is attributed to the deposition of calcium (Ca) due to differentiation of hBMSCs into osteogenic cells (Figures 3b,c and S15). Moreover, the alkaline phosphatase (ALP) activity for C_3N_4 sheets increases 12-fold with Alizarin red staining (Figure 3d) compared to the control groups. The von Kossa staining also indicates that the C_3N_4 sheets drastically increase the formation of mineralized nodules as compared to that of QCDs under light exposure (Figure S14).

Quantitative real-time PCR (qPCR) is used to detect expression levels of osteoblast marker genes such as ALP (an early stage maker gene), bone sialoprotein (BSP: a late stage maker gene), and osteocalcin (OCN: a late stage maker gene).

DOI: 10.1021/acsnano.6b07138
ACS Nano 2017, 11, 742–751

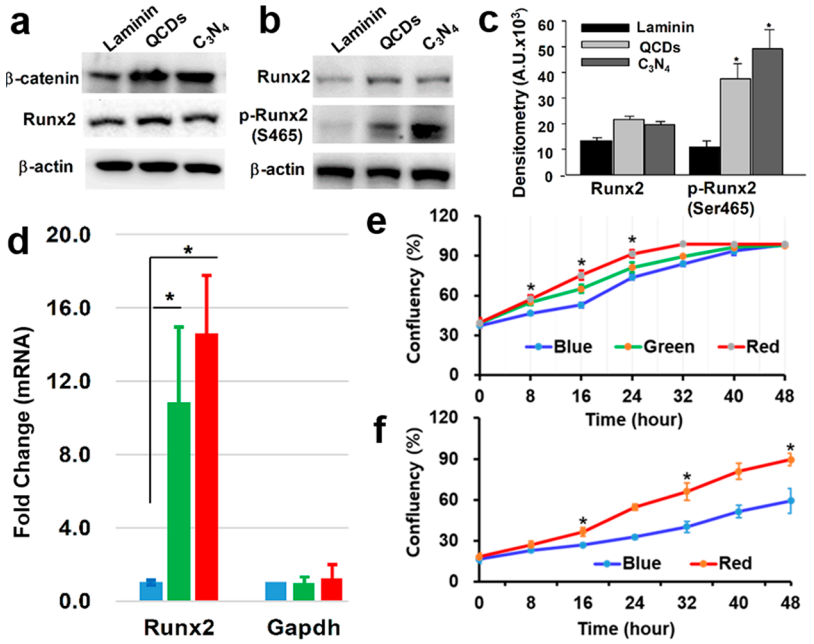

Figure 4. Dependence of C_3N_4 sheet-treated hBMSCs growth on light wavelength. (a) Whole cell lysates were analyzed to assess the hBMSC differentiation mechanism. (b) p-Runx2 was significantly enriched in nuclear fractions by QCDs and C_3N_4 sheets treatment. Equal amounts of protein were loaded. (c) Quantitative densitometry of the nuclear Runx2 and p-Runx2 normalized by β-actin protein. Data represent three separate observations (*$p < 0.05$). (d) Quantification of Runx2 expression after 14 days differentiation of hBMSCs under three different lights (blue, green, red). Gapdh denotes glyceraldehyde 3-phosphate dehydrogenase. (e) Growth curves for hBMSC grown in 96-well plates for 48 h. (f) Growth curves for BMSC grown without C_3N_4 as a negative control for (e). Every 8 h under different lights, the cells were counted using an IncuCyte live cell imager (ESSEN, USA). In (d–f) $n = 3$, *$p < 0.05$.

These mRNA levels were measured at different times and light conditions (Figure S16). These markers are well-known to be regulated by transcription factor, Runx 2. The levels of protein by Western blot (WB) and that of mRNA of Runx2 are in Figure 4. The activated Runx2 level is high enough to demonstrate osteogenic marker gene regulation. The expression levels increase dramatically as osteoblasts differentiate with respect to time. Upon irradiation, C_3N_4 sheets promote mRNA expression after 6 days (2.5-fold for ALP, 7-fold for BSP, and 3.5-fold for OCN compared to vitronectin (VTN)), while after 14 days, the BSP and OCN differentiations are further increased (13-fold and 21-fold, respectively) (Figure S16c,d). Similarly, QCDs induce the mRNA expressions of ALP, BSP, and OCN; however, these expressions are considerably lower than those obtained using C_3N_4 under light exposure. When red light is absorbed by C_3N_4 sheets, the emission of blue-light arising from two-photon absorption and the resulting small photocurrent in the nuclei and cytoplasm of hBMSCs induce inter and intracellular gradient charge forces. These forces may significantly influence the path and speed of bone matrix protein expression (ALP, BSP, and OCN).[29,37] Namely, an electric field is generated, and Ca^{2+} ion translocates through the cell-membrane voltage-gated calcium channels, leading to an increase in cystolic Ca^{2+} which results in an increase in activated calmodulin.[29] This promotes nucleotide synthesis and cellular proliferation. The calcium increase in response to carbon nitride treatment is likely to be due to the fact that the cytosolic calcium increases in Alizarin red S (ARS) staining and von Kossa test. ARS has been used for decades to evaluate calcium-rich deposits by cells in culture. Calcification occurs at nucleation sites known as matrix vesicles present in the lacunae of mineralizing cartilage. They are believed to accumulate Ca^{2+} and inorganic phosphate, which serve as nucleating agents for forming hydroxyapatite ($Ca_{10}(PO_4)_6(OH_2)_2$), the main inorganic component of bone. Usually after 10–14 days, the main inorganic component could be seen under a microscopy. The von Kossa (calcium stain) is intended for use in the histological visualization of calcium deposits in formalin fixed cells. This method is specific for calcium itself treated with a silver nitrate solution, and the silver is deposited by replacing the calcium reduced by the strong light, and so metallic silver is visualized. We demonstrated the effects of light on von Kossa staining. Both von Kossa and ARS staining allow simultaneous evaluation of mineral distribution and inspection of fine structures by phase contrast microscopy. ARS staining is particularly versatile in that the dye can be extracted from the stained monolayer and readily assayed.

We examined the expression level of β-catenin and Runx2, which is a canonical axis for osteoblast differentiation, to investigate the promotion of osteoblastic differentiation by C_3N_4 sheets.[38,39] Immunostaining hBMSCs on C_3N_4 sheets shows that large quantities of induced β-catenins and Runx2 are detected in the cytoplasm (Figure 4a), while phosphorylated-(p)-Runx2 (p-Runx2) is highly enriched in the nuclei (Figure 4b). The level of β-catenin and p-Runx2 induced by C_3N_4 suggests that Runx2 phosphorylation is regulated through a canonical Wnt signaling (Figure 4a–c). Since C_3N_4 sheets emit very strong PL around ~443 nm upon excitation at ~635 nm (Figure 2b), we next investigate whether different wavelengths have any effects on hBMSC differentiation. The hBMSCs are exposed to visible light using an LED array (Figure S17) (wavelength = 455 nm (blue), 520 nm (green), and 635 nm (red)). We compared different visible lights using an LED array mentioned in Figure S17 (wavelength = 455 nm (blue), 520 nm (green), and 635 nm (red)). All the light powers were same as 10 mA in 10 cm height. All dishes were covered to protect

DOI: 10.1021/acsnano.6b07138
ACS Nano 2017, 11, 742–751

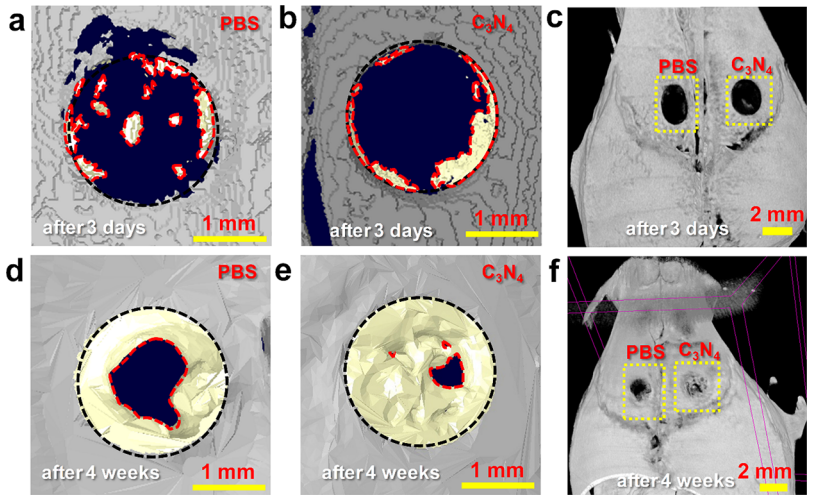

Figure 5. Comparison of PBS and C_3N_4 sheets for the enhancement in repairing cranial bone defect under red light *in vivo*. Analysis of bone regeneration in critical size cranial defects under red light. (a–f) 3D μ-CT images after 3 days or 4 weeks of PBS and C_3N_4 sheet-assisted treatments. Regenerated bone is indicated with a yellow color. Each figure is a representative example among 3 different experiments (n = 3). The results of QCDs are similar to that of PBS (see Figures 6 and 7).

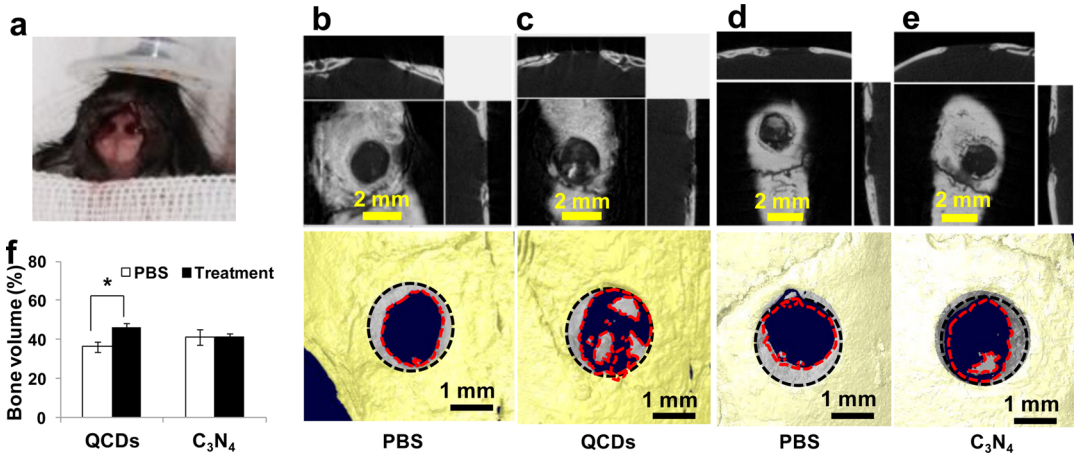

Figure 6. Evaluation of *in vivo* bone formation after 4 weeks in the absence of red light. (a) Photograph of mice. (b–e) The μ-CT images are analyzed to visualize and quantify bone regeneration in a PBS (b) *versus* QCDs (c) treated mouse as well as bone regeneration in a PBS (d) *versus* C_3N_4 sheets (e) treated mouse. The 3D images are reconstructed to illustrate the coronal section (top and right side of b) views of regenerated bone tissue. Gray areas in broken circles of lower panel images represent regenerated bone from the surgical margin of the calvarial defect. (f) The amount of new bone generated is evaluated by new bone volume in bone defects assessed from the projected area of the μ-CT images (*p < 0.02).

contamination, but well penetrated by these lights. The most significant proliferation and differentiation enhancements of hBMSCs are observed upon red-light irradiation of the cells grown on C_3N_4 sheets (Figure 4d). To determine the effect of red-light absorbance on hBMSC differentiation, mRNA levels of Runx2 were measured after 14 days cell growth and showed a 17-fold increase (Figure 4d). Under red light, the percentage of viable cells increases 3- to 4-fold compared to that of blue-light irradiation (Figure 4e,f). The absorption of red light by the C_3N_4 sheets leads to emission of broad blue PL to the cytoplasm of hBMSCs; this cell stimulation[18,19] influences the bone matrix protein expression (ALP, BSP, and OCN) and enhances osteogenic differentiation of hBMSCs.[40−42] It should be noted that blue/green-light irradiation was found to be much more effective in osteoblast differentiation of stem cells than red/yellow light irradiation or the dark condition.[28] In addition, the fast electron transfer and thermal transport properties of the C_3N_4 sheets could help in rapid and directed migration of the osteoblast precursor cells.[43,44]

In vivo bone regeneration in mouse cranial defects is performed using photoactive C_3N_4 sheets in the presence/absence of red light (Figures 5, 6, and S18; see also Bone Regeneration in a Mouse Cranial Defect Model in the Experimental Section). The μCT images of cranial defects were quantified at 4 weeks after surgery. Enhanced bone repair in response to C_3N_4 was shown as a percentage of new bone relative to the total defective sites (Figures 6 and 7). The restored area of the cranial defect increases from 19.6 ± 2.0% (after 3 days) to 91.1 ± 3.2% after 4 weeks using the photoactive C_3N_4 treatment. This is remarkable when compared to PBS treatment which shows 69.7 ± 2.9% recovery after 4 weeks (16.7 ± 1.1% after 3 days) (Figures 5a–f and S18b). The average new bone formations of the QCDs and C_3N_4 in the cranial defects are compared with the PBS treated defects in the absence and presence of red light (Figures 6 and

DOI: 10.1021/acsnano.6b07138
ACS Nano 2017, 11, 742–751

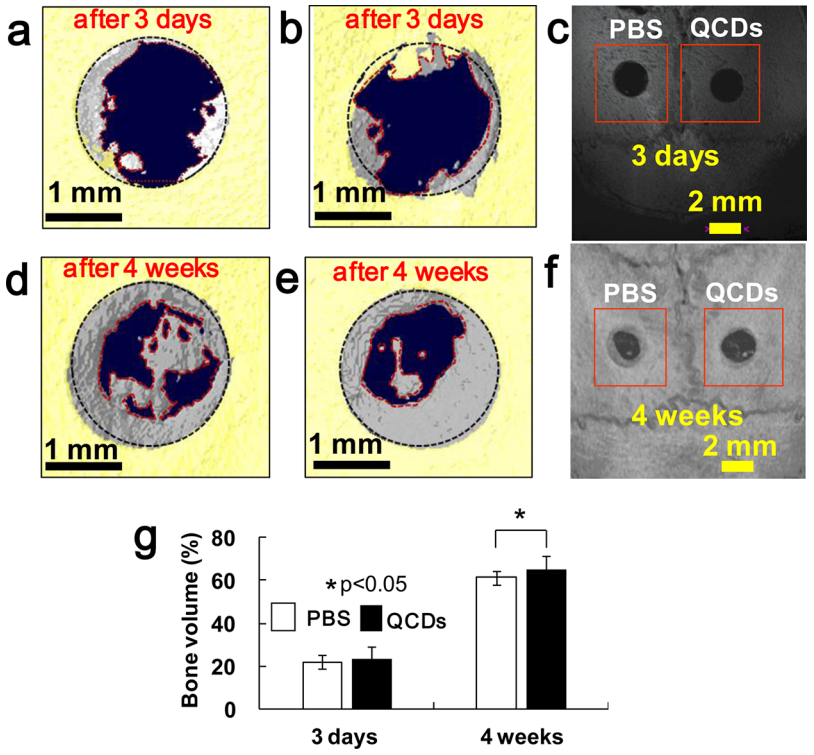

Figure 7. Comparison of PBS and QCDs for the enhancement in repairing the cranial bone defect under red light *in vivo*. Analysis of bone regeneration in critical size cranial defects under red light. (a–f) 3D μ-CT images after 3 days or 4 weeks of PBS- and QCD-assisted treatments. Each figure shows a representative example among 3 different experiments (n = 3). (G) The amount of new bone generated (*p < 0.05).

7). The experimental results (dark: C_3N_4: 41.3%, QCDs: 46.2%, PBS: 36.3%; light: C_3N_4: 91.1%, QCDs: 65.0%, PBS: 61.3%) demonstrate the importance of red-light absorption, in particular, in activating C_3N_4 sheets. The red light shows a synergistic effect:[37,38] (i) hBMSC differentiation with deep penetration of red light[10,11] into cellular membrane[24,45] (due to much deeper tissue penetration strength than the blue-light), resulting in rapid and directed migration of the osteoblast precursor cells[45] and (ii) the resulting cell stimulation (which enhances hBMSC differentiation) by photocurrent[29] upon red-light two-photon absorption of C_3N_4 sheets near nuclei (Figure 2g). This might activate a transduction signaling that leads to a change in redox status of the cytoplasm.[24,30,45] Consequently, this redox change would alter the Na^+/H^+ ratio (caused by an increase in ATPase activity), followed by a variation of Ca^{2+} flux.[24,30,45] The Ca^{2+} flux is reported to affect the levels of cyclic nucleotides that increase proliferation and osteogenic differentiation of hBMSCs and to augment mRNA expression.[24,30,45] These collective improvements would lead to enhancement of bone regeneration.

We address the recent trend of bone regeneration using three-dimensional (3D) plotting/direct ink writing.[46,47] There are some drawbacks arising from the utilization of toxic organic solvents, polymeric residues, *etc.* Furthermore, this 3D scaffolding techniques still require a longer period for the full bone regeneration than our present method. It might be possible that faster bone regeneration could occur by combining our method with 3D printing.

CONCLUDING REMARKS

Our findings in this work affirm the potential of C_3N_4 sheets in developing bone formation and directing hBMSCs toward bone regeneration. This efficient two-photon-assisted material approach could open opportunities toward the development of hBMSC-driven fracture repair treatments. Carbon nanotubes (CNTs) are often of micrometer size and nondispersible in water because carbon atoms in CNTs are not polarized. On the other hand, in the case of C_3N_4, not only is the sheet size <200 nm but also the C and N atoms are highly polarized with positive and negative charges, respectively. Thus, in contrast to hardly dispersible CNTs in water, small-sized C_3N_4 sheets are highly dispersible in water. Therefore, although CNTs are detrimental to red blood cells and can be accumulated in spleen and liver, highly dispersible small-sized carbon nitride can be easily washed away in spleen and liver. Indeed, according to cell viabilities assessed with MTT, Trypan Blue assay, and FACS analyses, the C_3N_4 shows no toxicity. Considering their high chemical stability and biologically less toxicity, C_3N_4 sheets could be suitable for the development of nanomaterials for biomolecules and other biomedical and clinical applications. Our data regarding the significance of application on living systems strongly support these concerns. To verify more detailed biological efficacy, more systemic approaches such as RNA expression profiling, proteomics, or metabolomic analyses on *in vivo* bone regeneration activity of C_3N_4 will be our next subjects to be further studied.

EXPERIMENTAL SECTION

Synthesis of C_3N_4 Sheets. Melamine ($C_3H_6N_6$) was heated at 600 °C for 3 h under argon with a ramp rate of 5 °C/min. The obtained yellow product was labeled as bulk C_3N_4 powder (Figure S1a). To obtain C_3N_4 sheets, as-prepared bulk C_3N_4 powder (100 mg) was dispersed in deionized (DI) water (100 mL) using sonication. The

DOI: 10.1021/acsnano.6b07138
ACS Nano 2017, 11, 742–751

resulting dispersion was milky in color (Figure S1b,ii) and was used without further treatment.

Synthesis of QCDs. In a typical synthesis, 2 g of ascorbic acid (AA) powder was placed in a 10 mL glass vial and then heated to 255 ± 5 °C in a heating mantle for 3 h (AA, Figure S3). On heating, the color of the AA powder changed from white to black. After cooling to room temperature, the product was added to DI water (100 mL) and sonicated for 1 h. The color of the obtained dispersion was clear yellow (Figure S1b,i). This color suggests the formation of QCDs. Finally, the dispersion was centrifuged at 10,000 rpm to remove large agglomerates and then further neutralized to pH = 7.0 with NaOH.

Characterization. The AFM samples were prepared by drop casting a few drops of an aqueous C_3N_4 dispersion onto a Si wafer. AFM images were determined using a Veeco Dimension 3100 Ambient AFM. Functional groups of the samples were analyzed by FTIR spectroscopy using a Varian 670, Agilent USA instrument. The structure of the samples was studied by analyzing XRD patterns, which were obtained using a high-power X-ray diffractometer (Rigaku, Japan). Additionally, structural information was obtained from XPS (Thermo Fisher, UK). The morphology of the products was characterized using field emission-scanning electron microscopy (FESEM, JEOL, FEG-XL 30S) and HRTEM (2100F, JEOL, Japan). UV−vis absorption spectra were obtained using a Shimadzu UV-2401PC spectrophotometer. The fluorescence properties were investigated using a Shanghi 756 MC UV−vis spectrometer and Shimadzu RF-5301 PC spectrofluoro-photometer. LED lights (wavelength = 455 nm (blue), 520 nm (green), and 635 nm (red)) were used for irradiation and exposure to cell viability. The distance was adjusted in such a way that the light intensity over a round spot of 2 cm^2 (area of the cell culture well) could be considered visually homogeneous. It is estimated that only three-quarters of the emitted power was utilized. The LED light was continuously turned on during the light exposure experiments.

Photocurrent Study. Photocurrent characterization was carried out in a three-electrode electrochemical cell. The powdered C_3N_4 sheets were coated on working electrode (graphite area 3.14 cm^2). The amount of catalysts is 1 mg/cm^2. A Pt wire and a Ag/AgCl/saturated NaCl reference electrode were used as the counter and reference electrodes, respectively. The applied potential is +0.8 V. The solution contains 0.5 M Na_2SO_4. The sample is illuminated with a broad-spectrum 300W xenon white lamp. The blue- and red-light shinning was controlled by filter.

QY Measurements. Absolute fluorescence QYs for QCDs and C_3N_4 sheets were measured using a high-resolution spectrofluorometer equipped with a single photon counting photomultiplier contained in a Peltier air-cooled house. Anthracene was used as a standard in the QY measurements. Typically, the QY was obtained by integrating the measured photon emission up to 600 nm using the following equation:

$$\Phi(\text{un}) = \{[\text{FLI(un)}/\text{abs(un)}] \times [\text{FLI(std)}/\text{abs(std)}]\} \times [n(\text{un})/n(\text{std})2] \times \Phi(\text{std})$$

where Φ(un) = QY of unknown; Φ(std) = QY of standard; FLI(un) = fluorescence of the unknown; FLI(std) = fluorescence of the standard; Abs(un) = absorbance of the unknown; Abs(std) = absorbance of the standard; n(un) = refractive index of solvent for the study of fluorescence and absorbance of the unknown sample; and n(std) = refractive index of neat solvent used in the standard sample.

***In Vitro* Cytotoxicity of C_3N_4 Sheets and QCDs.** *In vitro* cytotoxicities of C_3N_4 sheets and QCDs on human cervical cancer cells (HeLa) were investigated using a methyl thiazolyl tetrazolium (MTT) viability assay. Initially, HeLa cells were seeded into a 96-well U-bottom plate (90 μL $well^{-1}$) for 12 h. Subsequently, the cells were incubated with different concentrations of C_3N_4 sheets and QCDs (0, 25, 50, 100, and 200 μg mL^{-1}) for 48 h at 37 °C under 5% CO_2. After incubation, freshly prepared MTT (50 μL, 5 mg mL^{-1}) solution was poured into each well, and the plates were incubated for an additional 4 h. After removal of the medium, 150 μL of DMSO was added to the C_3N_4 sheets or QCDs treated cells, and these samples were vortexed for 15 min. Finally, the OD of the samples was evaluated at 500 nm using a microplate reader, and then the background subtraction at 690 nm was applied. The cell viability was calculated using the formula:

$$\text{cell viability}(\%) = \text{OD treated}/\text{OD control} \times 100\%$$

where OD control was obtained in the absence of C_3N_4 sheets and QCDs, and OD treated was obtained in the presence of the C_3N_4 sheets and QCDs. Each experiment was repeated 3 times, and the average data are presented.

Osteogenic Differentiation of hBMSCs. The hBMSCs were purchased from ATCC (ATCC PCS-500−012) and maintained in Dulbecco's modified eagle medium (DMEM) (Lonza) supplemented with 20% fetal bovine serum (FBS, Gibco BRL, Grand Island, NY), 100 units/mL penicillin, and 0.1 mg/mL streptomycin (Gibco BRL). The cell lines hBMSCs used in these experiments were identified by ATCC. The cell lines were authenticated to be multipotent hBMSCs and are capable of testing osteogenic proficiency. Before experiment, all cells are tested for mycoplasma.[48] For osteogenesis differentiation, hBMSCs were plated with an average concentration of 2×10^4 cells per well in four chamber slide plates. A schematic showing the experimental design and time course is given in Figure 3a. The four different types of slide plate preparation are displayed in Figure S13. Before plating the cells, the first chamber slides were coated with laminin molecules. The second and third slides were coated with laminin solutions (10 μg mL^{-1}) containing either QCDs (40 μg mL^{-1}) or C_3N_4 (40 μg mL^{-1}). The use of laminin is required so as to adhere the QCD or C_3N_4 sheets onto the glass slide surface. The fourth slide was designated as a control and as such was left uncoated. After 2 days, the hBMSCs were cultured using osteogenesis induction medium (OIM, 20% FBS, 10 mM β-glycerophosphate (USB Corp., Cleveland, OH), 50 μM ascorbate-2-phosphate (Sigma-Aldrich), and 100 nM dexamethasone (Sigma-Aldrich) in DMEM). The OIM medium was changed every 3 days. Cells were cultured at 37 °C in a humidified atmosphere containing 5% CO_2. In the case of illumination conditions, blue, green, and red LED lights were used during cell culture.

ARS Staining. To confirm mineral deposition by differentiated osteoblasts, cells were washed twice with PBS, placed in 4% paraformaldehyde for 20 min, washed twice with DI water, and then stained with a 1% ARS (Sigma−Aldrich) for 20 min. Cells were then washed three times with DI water and examined in the presence of calcium deposits, which were identified by the presence of red color. Mineral accumulation of differentiated osteoblasts was observed and photographed using a Zeiss Axiovert 135 microscope plus Olympus DP71 CCD camera (Olympus Corporation, Japan).

Determination of ALP Activity. Following culture, cells were lysed using protein lysis buffer (50 mM Tris-HCl (pH 7.5) and 0.1% TX-100). Cellular ALP activity was assayed colorimetrically by incubating cell lysates with the substrate *p*-nitrophenylphosphate (Sigma-Aldrich) in assay buffer (4 mM $MgCl_2$ (pH 10.5) and 200 mM 2-amino-2-methyl-1-phosphate) at 37 °C for 15 min. Absorbance was measured at 450 nm.

von Kossa Staining. The von Kossa (calcium stain) is intended for the visualization of calcium deposits in formalin fixed cells. The calcium recognition is based upon treatment with silver nitrate (ACS reagent, ≥ 99.0% Sigma-Aldrich) solution, wherein silver reduced by strong light replaces the calcium *via* deposition and can be visualized as metallic silver. Cells were washed with PBS and fixed with 10% formalin phosphate for 2 h, whereafter they were hydrated. After washing with distilled water 5 times, cells were incubated with 5% silver nitrate solution in a clear glass vial under UV light for 20 min, until nodules were black, and then the cells were washed in distilled water. The unreacted silver was removed with 5% sodium thiosulfate for 5 min and was washed again with distilled water 5 times. Cells were counterstained with toluidine blue 5% (Sigma-Aldrich, T3260) for 5 min. After washing with distilled water 5 times, images were gathered using microscopy.

mRNA Extraction and Real-Time qRT-PCR (Real-Time Quantitative Reverse Transcription PCR). RNA was extracted from hBMSCs using TRIzol reagent (Invitrogen, Grand Island, NY). cDNA was reverse-transcribed from 2 μg of the extracted cellular RNA

DOI: 10.1021/acsnano.6b07138
ACS Nano 2017, 11, 742−751

using oligo (dT) primers and Moloney murine leukemia virus reverse transcriptase (Promega, Madison, WI). Real-time qRT-PCR was performed using SYBR Green I Master mix (Roche, Indianapolis, IN) with a Roche Light Cycler 480 Real-Time PCR system. Real-time qRT-PCR conditions comprise a 10 min hot start at 95 °C, followed by 45 cycles of 15 s at 95 °C, 10 s at 60 °C, and 30 s at 72 °C. The following primers were used: human alkaline phosphatase (ALP) 5′-taacatcagggacattgacg-3′ (sense), 5′-tgcttgtatctcggtttgaa-3′ (antisense); human runt-related transcription factor 2 (Runx2) 5′-cagcctgcagcccggcaaaa-3′ (sense), 5′-cgcaaccggggcactgcag-3′ (antisense); human ribosomal protein large P0 (RPLP0) 5′-ggaatgtgggctttgtgttc-3′ (sense), 5′-tgcccctggagattttagtg-3′ (antisense). The expression levels of the mRNAs were normalized to the expression level of RPLP0 and compared.

Immunoblotting and Immunostaining. For immunoblotting, whole-cell lysates were prepared in lysis-buffer (50 mM Tris-HCl (pH 7.4), 150 mM NaCl, 1% TX-100, 1 mM EDTA, 1 mM EGTA, 50 mM NaF, 1 mM Na_3VO_4, 1 mM PMSF, and protease inhibitor cocktail (Sigma-Aldrich)). Lysates were then centrifuged at 14,000 rpm for 15 min (4 °C). A total of 20 μg of protein was separated by SDS-PAGE using 10% gels and transferred to nitrocellulose membranes. The membranes were blocked with 5% nonfat dry milk in Tween 20/Tris-buffered saline. For detection, the membranes were incubated with primary antibodies (polyclonal rabbit anti-Runx2, M-70, monoclonal anti-β-actin, sc-47778, Santa Cruz Biotechnologies, Santa Cruz, CA; A11037, Life tech, USA; IncuCyte live cell imager, ESSEN, USA) overnight at 4 °C. Horseradish peroxidase-conjugated secondary antibodies were incubated with the membrane for 1 h. Signals were visualized by chemiluminescence (ECL system, Amersham Biosciences, Piscataway, NJ). For immunostaining, nuclei were counterstained with Hoechst 33342 (Molecular Probes, Eugene, OR) according to the manufacturer's instructions.

Bone Regeneration in a Mouse Cranial Defect Model. Eight-week-old male mice (C57BL/6) were anesthetized with avertin (250 mg kg^{-1}) and rompun (10 mg kg^{-1}). After shaving the scalp hair, a 10 mm incision was made through the skin over the cranium, and full-thickness flaps were raised. Under sterile saline irrigation, two circular holes of 2.0 mm diameter were created in the mice cranium using a trephine bur (Ace Surgical Supply Co., USA). After the full-thickness of the cranial bone was removed, 20 μL of each C_3N_4 (0.1 mg/mL) or QCDs (0.1 mg mL^{-1}) with 20 μL Matrigel (Matrigel@Matrix, ThermoFisher, USA) were immediately placed in the defect. After 3 days for control measurement and 4 weeks later, the defective sites were analyzed with a 3D microcomputed (μCT) system (second Analysis Lab, Korea). For comparison, a negative group was created. In this group, a PBS solution with 20 μL Matrigel was implanted in the defect. We performed power analysis required to determine the sample size. The sample size was set to $n = 3$ per group for a power of 80% with a significance level of 0.05 to detect 50% difference between groups. In order to be allocated to test groups, each mouse was identified by ear punch; then the ID number was randomly assigned by "out of hat". Three groups of mice were anesthetized under Zoletil to create the cranial defects. The cranial bone defects (left and right cranial 2 defects/mice) were created using a trephine bur. Three days or 4 weeks after the surgery, the mice were analyzed to determine the amount of bone formation using a 3D μ-CT system. Codes for vehicle and reagents were blinded from technical personnel who performed animal experiments and analyses. The codes were revealed only after all experiments and the statistical analyses were accomplished. Animal study protocols were approved by the Institutional Animal Care and Use Committee at Ulsan National Institute of Science and Technology (no. UNISTIACUC-14-032).

Micro-CT Analysis. Four weeks after implantation, the animals were euthanized by CO_2 asphyxiation, and the skulls were harvested for analysis. Bone formation was evaluated with μ-CT scans ($n = 3$ per group). The μ-CT images were obtained using a μ-CT scanner (Bruker, SkyScan-1172, Belgium). The new bone volume was determined using the CT analyzer software: NRrecon, CTan, and CTvol (these programs are available on Internet Web sites supported by the Bruker company).

Statistical Analysis. All quantitative data from *in vivo* or *in vitro* were analyzed with a student t test to evaluate the variance of the statistical significance. We used the one-way analysis of variance (ANOVA) program (http://vassarstats.net) for independent or correlated samples. The values of $*p < 0.05$ and $** p < 0.01$ were considered to denote statistical significance.

ASSOCIATED CONTENT

Supporting Information

The Supporting Information is available free of charge on the ACS Publications website at DOI: 10.1021/acsnano.6b07138.

Additional text, analysis, and a table (PDF)

AUTHOR INFORMATION

Corresponding Authors

*E-mail: kimks@unist.ac.kr.

*E-mail: pgsuh@unist.ac.kr.

ORCID

Kwang S. Kim: 0000-0002-6929-5359

Author Contributions

‡These authors contributed equally.

Notes

The authors declare no competing financial interest.

ACKNOWLEDGMENTS

This work was supported by NRF (National Honor Scientist Program: 2010-0020414) and the Korea government (MSIP) (no. 2014M3A9D8034459).

REFERENCES

(1) Shi, D.; Xu, X.; Ye, Y.; Song, K.; Cheng, Y.; Di, J.; Hu, Q.; Li, J.; Ju, H.; Jiang, Q.; et al. Photo-Cross-Linked Scaffold with Kartogenin-Encapsulated Nanoparticles for Cartilage Regeneration. *ACS Nano* **2016**, *10*, 1292−1299.

(2) Zhang, X.; Zhang, C.; Lin, Y.; Hu, P.; Shen, Y.; Wang, K.; Meng, S.; Chai, Y.; Dai, X.; Liu, X.; et al. Nanocomposite Membranes Enhance Bone Regeneration Through Restoring Physiological Electric Microenvironment. *ACS Nano* **2016**, *10*, 7279−7286.

(3) Lewis, E. E. L.; Wheadon, H.; Lewis, N.; Yang, J.; Mullin, M.; Hursthouse, A.; Stirling, D.; Dalby, M. J.; Berry, C. C. A Quiescent, Regeneration-Responsive Tissue Engineered Mesenchymal Stem Cell Bone Marrow Niche Model *via* Magnetic Levitation. *ACS Nano* **2016**, *10*, 8346−8354.

(4) Xavier, J. R.; Thakur, T.; Desai, P.; Jaiswal, M. K.; Sears, N.; Cosgriff-Hernandez, E.; Kaunas, R.; Gaharwar, A. K. Bioactive Nanoengineered Hydrogels for Bone Tissue Engineering: A Growth-Factor-Free Approach. *ACS Nano* **2015**, *9*, 3109−3118.

(5) Min, J.; Choi, K. Y.; Dreaden, E. C.; Padera, R. F.; Braatz, R. D.; Spector, M.; Hammond, P. T. Designer Dual Therapy Nanolayered Implant Coatings Eradicate Biofilms and Accelerate Bone Tissue Repair. *ACS Nano* **2016**, *10*, 4441−4450.

(6) Orlic, D.; Kajstura, J.; Chimenti, S.; Jakoniuk, I.; Anderson, S. M.; Li, B.; Pickel, J.; McKay, R.; Nadal-Ginard, B.; Bodine, D. M.; et al. Bone Marrow Cells Regenerate Infarcted Myocardium. *Nature* **2001**, *410*, 701−705.

(7) Grayson, W. L.; Bunnell, B. A.; Martin, E.; Frazier, T.; Hung, B. P.; Gimble, J. M. Stromal Cells and Stem Cells in Clinical Bone Regeneration. *Nat. Rev. Endocrinol.* **2015**, *11*, 140−150.

(8) Kim, J. M.; Shin, H.-I.; Cha, S.-S.; Lee, C. S.; Hong, B. S.; Lim, S.; Jang, H.-J.; Kim, J.; Yang, Y. R.; Kim, Y.-H.; et al. DJ-1 Promotes Angiogenesis and Osteogenesis by Activating FGF Receptor-1 Signaling. *Nat. Commun.* **2012**, *3*, 1296.

(9) Lutolf, M. P.; Gilbert, P. M.; Blau, H. M. Designing Materials to Direct Stem-Cell Fate. *Nature* **2009**, *462*, 433−441.

DOI: 10.1021/acsnano.6b07138
ACS Nano 2017, 11, 742−751

(10) Xu, Y.; Shi, Y.; Ding, S. A Chemical Approach to Stem-Cell Biology and Regenerative Medicine. *Nature* **2008**, *453*, 338−344.
(11) Guan, M.; Yao, W.; Liu, R.; Lam, K. S.; Nolta, J.; Jia, J.; Panganiban, B.; Meng, L.; Zhou, P.; Shahnazari, M.; et al. Directing Mesenchymal Stem Cells to Bone to Augment Bone Formation and Increase Bone Mass. *Nat. Med.* **2012**, *18*, 456−462.
(12) Neffe, A. T.; Pierce, B. F.; Tronci, G.; Ma, N.; Pittermann, E.; Gebauer, T.; Frank, O.; Schossig, M.; Xu, X.; Willie, B. M.; et al. One Step Creation of Multifunctional 3D Architectured Hydrogels Inducing Bone Regeneration. *Adv. Mater.* **2015**, *27*, 1738−1744.
(13) Shen, L. H.; Li, Y.; Chen, J.; Cui, Y.; Zhang, C.; Kapke, A.; Lu, M.; Savant-Bhonsale, S.; Chopp, M. One-Year Follow-Up After Bone Marrow Stromal Cell Treatment in Middle-Aged Female Rats with Stroke. *Stroke* **2007**, *38*, 2150−2156.
(14) Chimene, D.; Alge, D. L.; Gaharwar, A. K. Two-Dimensional Nanomaterials for Biomedical Applications: Emerging Trends and Future Prospects. *Adv. Mater.* **2015**, *27*, 7261−7284.
(15) Yin, P. T.; Shah, S.; Chhowalla, M.; Lee, K. B. Design, Synthesis, and Characterization of Graphene-Nanoparticle Hybrid Materials for Bioapplications. *Chem. Rev.* **2015**, *115*, 2483−2531.
(16) Kajiya, H.; Katsumata, Y.; Sasaki, M.; Tsutsumi, T.; Kawaguchi, M.; Fukushima, T. Photothermal Stress Triggered by Near-Infrared-Irradiated Carbon Nanotubes Up-Regulates Osteogenesis and Mineral Deposition in Tooth-Extracted Sockets. *Int. J. Hyperthermia* **2015**, *31*, 635−642.
(17) La, W. G.; Jin, M.; Park, S.; Yoon, H. H.; Jeong, G. J.; Bhang, S. H.; Park, H.; Char, K.; Kim, B. S. Delivery of Bone Morphogenetic Protein-2 and Substance P Using Graphene Oxide for Bone Regeneration. *Int. J. Nanomed.* **2014**, *9*, 107−116.
(18) Yanagi, T.; Kajiya, H.; Kawaguchi, M.; Kido, H.; Fukushima, T. Photothermal Stress Triggered by Near Infrared-Irradiated Carbon Nanotubes Promotes Bone Deposition in Rat Calvarial Defects. *J. Biomater. Appl.* **2015**, *29*, 1109−1118.
(19) Park, J. K.; Kim, Y. J.; Yeom, J. S.; Jeon, J. H.; Yi, G. C.; Je, J. H.; Hahn, S. K. The Topographic Effect of Zinc Oxide Nanoflowers on Osteoblast Growth and Osseointegration. *Adv. Mater.* **2010**, *22*, 4857−4861.
(20) Park, J. K.; Shim, J. H.; Kang, K. S.; Yeom, J. S.; Jung, H. S.; Kim, J. Y.; Lee, K. H.; Kim, T. H.; Kim, S. Y.; Cho, D. W.; et al. Solid Free-Form Fabrication of Tissue-Engineering Scaffolds with a Poly(lactic-co-glycolic acid) Grafted Hyaluronic Acid Conjugate Encapsulating an Intact Bone Morphogenetic Protein−2/Poly-(ethylene glycol) Complex. *Adv. Funct. Mater.* **2011**, *21*, 2906−2912.
(21) Jung, H. S.; Kong, W. H.; Sung, D. K.; Lee, M.-Y.; Beack, S. E.; Keum, D. H.; Kim, K. S.; Yun, S. H.; Hahn, S. K. Nanographene Oxide−Hyaluronic Acid Conjugate for Photothermal Ablation Therapy of Skin Cancer. *ACS Nano* **2014**, *8*, 260−268.
(22) Park, J.; Kim, B.; Han, J.; Oh, J.; Park, S.; Ryu, S.; Jung, S.; Shin, J.-Y.; Lee, B. S.; Hong, B. H.; et al. Graphene Oxide Flakes as a Cellular Adhesive: Prevention of Reactive Oxygen Species Mediated Death of Implanted Cells for Cardiac Repair. *ACS Nano* **2015**, *9*, 4987−4999.
(23) Kang, S.; Park, J. B.; Lee, T. J.; Ryu, S.; Bhang, S. H.; La, W. G.; Noh, M. K.; Hong, B. H.; Kim, B. S. Covalent Conjugation of Mechanically Stiff Graphene Oxide Flakes to Three-Dimensional Collagen Scaffolds for Osteogenic Differentiation of Human Mesenchymal Stem Cells. *Carbon* **2015**, *83*, 162−172.
(24) Li, J. L.; Bao, H. C.; Hou, X. L.; Sun, L.; Wang, X. G.; Gu, M. Graphene Oxide Nanoparticles as a Nonbleaching Optical Probe for Two-Photon Luminescence Imaging and Cell Therapy. *Angew. Chem., Int. Ed.* **2012**, *51*, 1830−1834.
(25) Smith, K. C. The Photobiological Basis of Low Level Laser Radiation Therapy. *Laser Therapy* **1991**, *3*, 19−24.
(26) Whelan, H. T.; Smits, R. L., Jr.; Buchman, E. V.; Whelan, N. T.; Turner, S. G.; Margolis, D. A.; Cevenini, V.; Stinson, H.; Ignatius, R.; Martin, T.; et al. Effect of NASA Light-Emitting Diode Irradiation on Wound Healing. *J. Hematother.* **2001**, *19*, 305−314.
(27) Li, W. T.; Leu, Y. C.; Wu, J. L. Red-Light Light-Emitting Diode Irradiation Increases the Proliferation and Osteogenic Differentiation of Rat Bone Marrow Mesenchymal Stem Cells. *Photomed. Laser Surg.* **2010**, *28*, S157−S165.
(28) Li, W. T.; Chen, H. L.; Wang, C. T. Effect of Light Emitting Diode Irradiation on Proliferation of Human Bone Marrow Mesenchymal Stem Cells. *J. Med. Biol. Eng.* **2005**, *26*, 35−42.
(29) Jin, G.; Prabhakaran, M. P.; Liao, S.; Ramakrishna, S. Photosensitive Materials and Potential of Photocurrent Mediated Tissue Regeneration. *J. Photochem. Photobiol., B* **2011**, *102*, 93−101.
(30) Khabashesku, V. N.; Zimmerman, J. L.; Margrave, J. L. Powder Synthesis and Characterization of Amorphous Carbon Nitride. *Chem. Mater.* **2000**, *12*, 3264−3270.
(31) Haase, M.; Schäfer, H. Upconverting Nanoparticles. *Angew. Chem., Int. Ed.* **2011**, *50*, 5808−5829.
(32) Jia, X.; Li, J.; Wang, E. One-Pot Green Synthesis of Optically pH-Sensitive Carbon Dots with Upconversion Luminescence. *Nanoscale* **2012**, *4*, 5572−5575.
(33) Liu, Q.; Guo, B. D.; Rao, Z. Y.; Zhang, B. H.; Gong, J. R. Strong Two-Photon-Induced Fluorescence From Photostable, Biocompatible Nitrogen-Doped Graphene Quantum Dots for Cellular and Deep-Tissue Imaging. *Nano Lett.* **2013**, *13*, 2436−2441.
(34) Zhang, X.; Xie, X.; Wang, H.; Zhang, J.; Pan, B.; Xie, Y. Enhanced Photoresponsive Ultrathin Graphitic-Phase C_3N_4 Nanosheets for Bioimaging. *J. Am. Chem. Soc.* **2013**, *135*, 18−21.
(35) Stoddart, M. J. *Mammalian Cell Viability: Methods & Protocols, Methods in Molecular Biology*; Springer Protocols: New York, 2011; Vol. *740*.
(36) Scheiman, J.; Jamieson, K. V.; Ziello, J.; Tseng, J.-C.; Meruelo, D. Extraribosomal Functions Associated with the C Terminus of the 37/67 kDa Laminin Receptor are Required for Maintaining Cell Viability. *Cell Death Dis.* **2010**, *1*, e42.
(37) Petecchia, L.; Sbrana, F.; Utzeri, R.; Vercellino, M.; Usai, C.; Visai, L.; Vassalli, M.; Gavazzo, P. Electro-Magnetic Field Promotes Osteogenic Differentiation of BM-hMSCs Through a Selective Action on Ca^{2+}-Related Mechanisms. *Sci. Rep.* **2015**, *5*, 13856.
(38) Komori, T. Regulation of Skeletal Development by the Runx Family of Transcription Factors. *J. Cell. Biochem.* **2005**, *95*, 445−453.
(39) Gaur, T.; Lengner, C. J.; Hovhannisyan, H.; Bhat, R. A.; Bodine, P.V. N.; Komm, B. S.; Javed, A.; van Wijnen, A. J.; Stein, J. L.; Stein, G. S.; et al. Canonical WNT Signaling Promotes Osteogenesis by Directly Stimulating Runx2 Gene Expression. *J. Biol. Chem.* **2005**, *280*, 33132−33140.
(40) Mendez-Ferrer, S.; Michurina, T. V.; Ferraro, F.; Mazloom, A. R.; MacArthur, B. D.; Lira, S. A.; Scadden, D. T.; Ma'ayan, A.; Enikolopov, G. N.; Frenette, P. S. Mesenchymal and Haematopoietic Stem Cells Form a Unique Bone Marrow Niche. *Nature* **2010**, *466*, 829−834.
(41) D'Errico, J. A.; MacNeil, R. L.; Takata, T.; Berry, J.; Strayhorn, C.; Somerman, M. J. Expression of Bone Associated Markers by Tooth Root Lining Cells, *In Situ* and *In Vitro*. *Bone* **1997**, *20*, 117−126.
(42) Harada, S.; Rodan, G. A. Control of Osteoblast Function and Regulation of Bone Mass. *Nature* **2003**, *423*, 349−355.
(43) Banks, T. A.; Luckman, P. S. B.; Frith, J. E.; Cooper-White, J. J. Effects of Electric Fields on Human Mesenchymal Stem Cell Behaviour and Morphology Using a Novel Multichannel Device. *Integr. Biol.* **2015**, *7*, 693−712.
(44) Naderi-Meshkin, H.; Bahrami, A. R.; Bidkhori, H. R.; Mirahmadi, M.; Ahmadiankia, N. Strategies to Improve Homing of Mesenchymal Stem Cells for Greater Efficacy in Stem Cell Therapy. *Cell Biol. Int.* **2015**, *39*, 23−34.
(45) Friedmann, H.; Lubart, R.; Laulicht, I.; Rochkind, S. A Possible Explanation of Laser Induced Stimulation and Damage of Cell Culture. *J. Photochem. Photobiol., B* **1991**, *11*, 87−91.
(46) Zhang, X. J.; Li, Y.; Chen, Y. E.; Chen, J. H.; Ma, P. X. Cell-Free 3D Scaffold with Two-Stage Delivery of miRNA-26a to Regenerate Critical-Sized Bone Defects. *Nat. Commun.* **2016**, *7*, 10376.
(47) Bose, S.; Vahabzadeh, S.; Bandyopadhyay, A. Bone Tissue Engineering Using 3D Printing. *Mater. Today* **2013**, *16*, 496−504.

DOI: 10.1021/acsnano.6b07138
ACS Nano 2017, 11, 742−751

(48) Lincoln, C. K.; Gabridge, M. G. Cell Culture Contamination: Sources, Consequences, Prevention, and Elimination. *Methods Cell Biol.* **1998**, *57*, 49−65.

DOI: 10.1021/acsnano.6b07138
ACS Nano 2017, 11, 742−751